electronics

Article

Comparative Performance Evaluation of Conventional and Folded Detector Structures: Application to Perovskite X-ray Detectors

Robin Ray and M. Z. Kabir *

Department of Electrical and Computer Engineering, Concordia University, 1455 Boul. de Maisonneuve Ouest, Montréal, QC H3G 1M8, Canada; robin.ray@concordia.ca
* Correspondence: zahangir.kabir@concordia.ca

Abstract: The imaging performance of a semiconductor radiation imaging detector critically depends on its photoconductor layer thickness. The conventional detector structure (i.e., a photoconductor layer is sandwiched between two parallel electrodes) needs a strict design criterion on photoconductor thickness as compared to folded detector structure for optimizing the detective quantum efficiency (DQE), which is the most important imaging performance. In this paper, the DQE performance of both folded and conventional detector structures is analyzed by incorporating the quantum noise due to random charge carrier trapping in the photoconductor layer in the cascaded linear system model. An analytical expression for the variance of incomplete charge collection in folded structure is also developed. The optimum values of photoconductor layer thickness and spacing between electrodes for maximizing the DQE under various combinations of exposure, electronic noise and charge carrier transport parameters are investigated. The folded structure provides a design flexibility for achieving DQE higher than 0.7 by adjusting the distance between electrodes without compromising the quantum efficiency while the maximum possible DQE in conventional structure can be even below 0.3 for certain values of material and detector parameters.

Keywords: perovskite X-ray detector; detective quantum efficiency; conventional and folded detector structures; flat-panel X-ray imagers; photoconductive detectors

Citation: Ray, R.; Kabir, M.Z. Comparative Performance Evaluation of Conventional and Folded Detector Structures: Application to Perovskite X-ray Detectors. *Electronics* **2023**, *12*, 2976. https://doi.org/10.3390/electronics12132976

Academic Editor: Hector E. Nistazakis

Received: 30 May 2023
Revised: 2 July 2023
Accepted: 3 July 2023
Published: 6 July 2023

1. Introduction

X-ray photoconductor-based flat-panel X-ray imagers (FPXIs) produce superior X-ray image as compared to scintillator-based detectors and are the commercially available digital X-ray detectors for mammography [1,2]. These detectors are, at present, under scrutiny for use in general radiography, fluoroscopy, tomosynthesis and portal imaging [3,4]. Amorphous selenium (*a*-Se) is the most successful photoconductor for photoconductor-based X-ray detectors because it can be conveniently deposited over large area at low-temperature and *a*-Se based detectors show low dark current and good charge-transport properties. There is one important drawback of *a*-Se, which is its lower intrinsic X-ray sensitivity (i.e., its large ionization energy, W_i, which is the minimum radiation energy required to create a single electron-hole pair, EHP) as compared to other X-ray photoconductors such as polycrystalline HgI_2 or CdZnTe [5]. For example, the value of W_i in *a*-Se is about 45 eV at the typical operating the electric field of 10 V/μm whereas the value of W_i is 5–6 eV for other X-ray photoconductors. Lower W_i provides more EHP generation and improves the signal strength (i.e., higher X-ray sensitivity) and signal to noise ratio. However, the basic underlying problem with most of these polycrystalline detectors is that they exhibit either an unacceptably large dark current (a current that flows in the detector in absence of irradiation) or they possesses significantly low charge collection efficiency [5,6]. There has been an active search going on to find efficient alternate X-ray photoconductors [5].

The use of Hybrid Organic−Inorganic Perovskites (HOIPs) in large area X-ray imaging detectors was first realized in 2015 when Yakunin et al. [7] first demonstrated a prototype X-ray detector using a thick layer (~100 µm) of polycrystalline methylammonium lead iodide (poly-$MAPbI_3$ where MA is CH_3NH_3) perovskite photoconductor. This initial prototype detector showed a very high dark current. Later, Kim et al. [8] proposed a multilayer structure using blocking layers to poly-$MAPbI_3$ detectors to reduce the dark current. Their structure showed reasonably low dark current, good X-ray sensitivity but very poor resolution in terms of the modulation transfer function (MTF). Deumel et al. [9] reported slightly better resolution in their 230 µm thick $MAPbI_3$ detector. Recently, Y. Li [10] et al. demonstrated much lower dark current in their perovskite detector structures.

The photoconductor layer thickness plays a very important role in conventional detector structure (i.e., a photoconductor layer is sandwiched between two electrodes where charges are collected in corresponding pixels) on imaging performances [5,8]. A relatively thicker layer is required for better sensitivity. However, the thicker layer contributes to more noise and signal spreading as carriers must travel a longer distance to reach the electrodes, and thus adversely affects image resolution and detective quantum efficiency (DQE) [11,12]. Recently, Mescher et al. [13] proposed a folded structure where charge carriers travel perpendicular to the direction of incident X-rays. Note that the charge carrier transport mechanism in folded structure is similar to a co-planar detector structure [14]. In folded structure the X-ray quantum efficiency can be improved using a thicker layer without affecting the charge collection by keeping the charge collecting electrodes at a reasonable distance. They theoretically analyzed the DQE using an oversimplified analytical model. In their model, they didn't consider the quantum noise due to random nature of charge carrier trapping, which is a very important factor for accurate modeling of the detective quantum efficiency [15].

In this paper, we have analyzed the detective quantum efficiency of both folded and conventional detector structures by incorporating the quantum noise due to random charge carrier trapping. We have developed an analytical expression for the variance of charge collection in folded structure. The folded structure provides more design flexibility for optimum DQE. The optimum values of photoconductor layer thickness and spacing between electrodes for maximizing the DQE under various material parameters and detector operating conditions are investigated.

2. Theory

The DQE measures the relative change of signal to noise ratio from its input to its output through various stages of an imaging system. The X-ray image can be degraded by various sources of stochastic and deterministic signal fluctuations which arise along the imaging chain. The DQE is expressed quantitatively as

$$\mathrm{DQE} = \frac{\mathrm{SNR}_{\mathrm{out}}^2}{\mathrm{SNR}_{\mathrm{in}}^2}, \tag{1}$$

where $\mathrm{SNR}_{\mathrm{in}}$ and $\mathrm{SNR}_{\mathrm{out}}$ are the signal to noise ratio at the input and output stages of an image detector, respectively.

2.1. Conventional Planner Structure

The conventional detector structure, a photoconductor layer has been sandwiched between two large area parallel plate electrodes and a bias voltage is applied between the two electrodes to establish an electric field *F*, is shown in Figure 1.

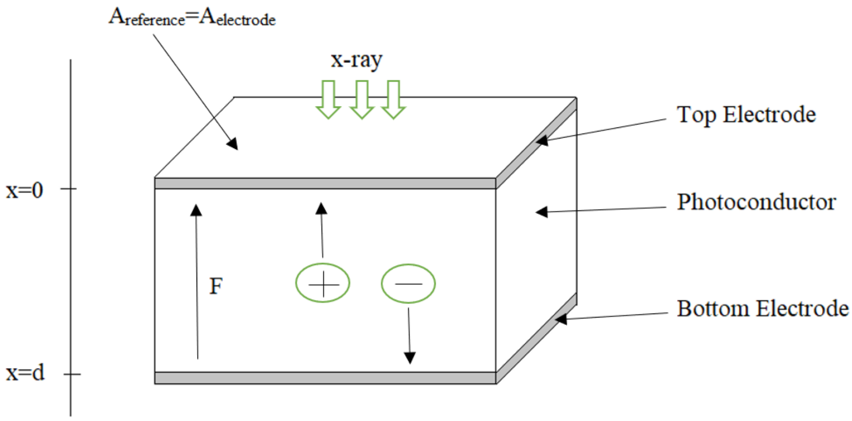

Figure 1. A conventional detector structure for negatively biased top electrode.

The DQE performance of many imaging systems is usually analyzed by developing a cascaded linear system model in which the imaging system is described as cascades of simple and independent elementary stages. The cascaded linear system model for calculating DQE (without considering signal spreading) of a detector that is shown in Figure 2 consists of four stages: (1) X-ray attenuation, (2) the creation of EHPs (conversion gain), (3) charge collection process, and (4) the addition of electronic noise. The flow chart shown in Figure 2 illustrates the signals and noise power after every stage. Since the spatial spreading of signal and noise are not considered, the DQE analysis in this work represents the zero spatial frequency detective quantum efficiency DQE.

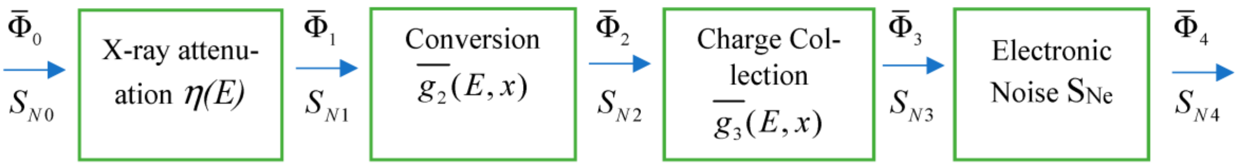

Figure 2. Cascaded linear system model for a conventional detector structure.

Each of the first three stages is defined as a stochastic gain stage. For the stochastic gain stage i the output mean signal quanta and noise power spectrum (NPS) per unit area arising from incident X-ray photon interactions at depth x from the radiation-receiving electrode are, respectively [16],

$$\overline{\Phi}_i(E,x) = \overline{g}_i(E,x)\overline{\Phi}_{i-1}(E,x) \tag{2}$$

$$S_{N_i}(E,x) = \overline{g}_i^2(E,x)S_{N(i-1)}(E,x) + \sigma_{g_i}^2(E,x)\overline{\Phi}_{i-1}(E,x) \tag{3}$$

where E is the incident X-ray photon energy, $\overline{\Phi}_{i-1}(E,x)$ and $S_{N(i-1)}(E,x)$ are the mean number of quanta and the NPS incident on stage i, respectively, and $\overline{g}_i(E,x)$ and $\sigma_{gi}{}^2(E,x)$ are the mean gain and variance of the gain of the ith stage. The first term in Equation (3) represents the amplification of the quantum noise and the second term represents an additional noise due to the random fluctuation of the amplification gain of the ith stage. Following the flow chart in Figure 2, the mean gain and the variance of gain of each stage are determined as follows.

The gain of the X-ray attenuation stage is the quantum efficiency η of the detector, which is given by,

$$\eta(E) = 1 - e^{-\alpha d}, \tag{4}$$

where E is the incident X-ray photon energy, $\alpha(E)$ and d are the linear attenuation coefficient and the distance between two electrodes (which is the same as the photoconductor layer thickness), respectively. An incident X-ray photon on this selection stage either interacts with the detector, probability η, or does not, probability $(1-\eta)$. Therefore, this is a binary selection process [17]. According to the binomial theorem, the variance of η,

$$\sigma_{g1}^2 = \eta(1-\eta).$$

The mean conversion gain $\overline{g}_2(E,x)$ of the second stage represents the mean number of EHPs generated after the absorption of an X-ray photon interaction at x is,

$$\overline{g}_2(E,x) = \frac{E_{ab}(E,x)}{W_i}, \tag{5}$$

where $E_{ab}(E,x)$ is the average absorbed energy per X-ray photon of energy E. For a relatively thinner detector, the reabsorption probability of the secondary photons is small and thus $E_{ab}(E) \approx (\alpha_{en}/\alpha)E$, where α_{en} is the energy absorption coefficient of the photoconductor. On the other hand, the secondary photons are mostly reabsorbed in a thicker detector (i.e., in detectors with high η) and thus, $E_{ab} \approx E$.

There is a fluctuation in conversion gain due to the stochastic fluctuation of the number of EHP generation per X-ray photon. We assume that the mean number of free EHPs released per X-ray photon obeys a Poisson process, i.e., $\sigma_{g_2}^2(E) \approx \overline{g}_2(E)$ [16,18].

The electric field remains relatively uniform across the photoconductor layer and bimolecular recombination is negligible in small signals, which is quite appropriate for medical diagnostic applications [19]. The diffusion of carriers is negligible compared with their drift counterpart because of relatively high applied fields across the photoconductor. The general transport behavior in many photoconductors can be described in terms of a constant drift mobility μ and a single carrier lifetime τ for each type of carriers (holes and electrons) [16]. With these assumptions above, the average charge collection efficiency, $\overline{g}_3(x)$, at the electrodes from EHP generation at coordinate x can be written as [20],

$$\overline{g}_3(x) = x_t(1-e^{-\frac{x}{dx_t}}) + x_b(1-e^{-\frac{d-x}{dx_b}}) \tag{6}$$

where $x_t = \mu_t\tau_t F/d$, $x_b = \mu_b\tau_b F/d$. The subscript t and b refer to carrier types drifting to the top and bottom electrodes respectively; the top electrode receives the X-ray radiation. The variance of charge collection due to random trapping for an EHP generation at x is given by [15],

$$\sigma_{g_3}{}^2(x) = x_t{}^2 + x_b{}^2 - x_t{}^2e^{-\frac{2x}{dx_t}} - x_b{}^2e^{-\frac{2(d-x)}{dx_b}} - 2x_t\frac{x}{d}e^{-\frac{x}{dx_t}} - 2x_b(1-\frac{x}{d})e^{-\frac{d-x}{dx_b}} \tag{7}$$

During image readout, the image signal passes through TFT/CMOS switch and charge amplifiers and thus the equivalent electronic noise power S_{Ne} associated with these electronic components is added to the total noise power [12].

The input noise in the number of X-ray quanta incident on the detector is usually considered to follow a Poisson process and thus the input NPS is $S_{\mathrm{N0}} = \overline{\Phi}_0$, where $\overline{\Phi}_0$ is the mean number of incident X-ray photons per unit area. Thus, the square of signal to noise ratio at the input,

$$\mathrm{SNR}_{\mathrm{in}}^2 = \overline{\Phi}_0. \tag{8}$$

The X-rays are attenuated exponentially across the photoconductor thickness. Therefore, the probability density function for an X-ray photon, that is attenuated within a detector, to interact at a distance x from the top electrode is,

$$P_x(x) = \frac{\alpha}{\eta}e^{-\alpha x}\,; 0 \le x \le d \tag{9}$$

Applying Equations (2) and (3) successively, the expected total signal at the output of the third stage is,

$$\overline{\Phi}_3 = \eta\overline{\Phi}_0\overline{g}_2\int_0^d \overline{g}_3(x)p_x(x)dx = \eta\overline{\Phi}_0\overline{g}_2\overline{\eta}_{cc} \tag{10}$$

where the average charge collection efficiency,

$$\overline{\eta}_{cc} = x_t\left\{1 - \frac{1-e^{-\frac{1}{\Delta}-\frac{1}{x_t}}}{\left(1-e^{-\frac{1}{\Delta}}\right)\left(1+\frac{\Delta}{x_t}\right)}\right\} + x_b\left\{1 + \frac{e^{-\frac{1}{x_b}} - e^{-\frac{1}{\Delta}}}{\left(1-e^{-\frac{1}{\Delta}}\right)\left(\frac{\Delta}{x_b}-1\right)}\right\} \tag{11}$$

Similarly, the NPS at the output of third stage is,

$$S_{N3} = \overline{\Phi}_0\eta\overline{g}_2\int_0^d \left\{\overline{g}_3^2(x)[1+\overline{g}_2] + \sigma_{g_3}{}^2(x)\right\}P_x(x)dx, \tag{12}$$

$$\begin{aligned} S_{N3} = {}& \eta\overline{\Phi}_0\overline{g}_2(\overline{g}_2+1)\left[x_t{}^2(1+x_tA) + 2x_tx_bB + x_b{}^2(1+x_bC)\right] \\ &+\eta\overline{\Phi}_0\overline{g}_2\left[x_t{}^2(1+D) + x_b{}^2(1+E) + x_t{}^3F + x_b{}^3G\right] \end{aligned} \tag{13}$$

where,

$$A = 2\eta_a(e^{-\frac{1}{x_t}-\frac{1}{\Delta}}-1) - \eta_b(e^{-\frac{2}{x_t}-\frac{1}{\Delta}}-1),$$

$$B = 1 + x_t\eta_a\left(e^{-\frac{1}{x_t}-\frac{1}{\Delta}}-1\right) - x_b\eta_c\left(e^{-\frac{1}{\Delta}} - e^{-\frac{1}{x_b}}\right) + x_tx_b\eta_e\left(e^{-\frac{1}{x_t}-\frac{1}{\Delta}} - e^{-\frac{1}{x_b}}\right),$$

$$C = \eta_d\left(e^{\frac{1}{\Delta}} - e^{-\frac{2}{x_b}}\right) - 2\eta_c\left(e^{-\frac{1}{\Delta}} - e^{-\frac{1}{x_b}}\right),$$

$$D = 2\eta_a e^{-\frac{1}{x_t}-\frac{1}{\Delta}},$$

$$E = 2\eta_c e^{-\frac{1}{x_b}},$$

$$F = \eta_b\left(e^{-\frac{2}{x_t}-\frac{1}{\Delta}}-1\right) - 2\eta_f\left(1-e^{-\frac{1}{x_t}-\frac{1}{\Delta}}\right),$$

$$G = -\eta_d\left(e^{-\frac{1}{\Delta}} - e^{-\frac{2}{x_b}}\right) - 2\eta_g\left(e^{-\frac{1}{\Delta}} - e^{-\frac{1}{x_b}}\right),$$

$$\eta_a = \frac{1}{\eta\Delta\left(1+\frac{x_t}{\Delta}\right)},\ \eta_b = \frac{1}{\eta\Delta\left(2+\frac{x_t}{\Delta}\right)},$$

$$\eta_c = \frac{1}{\eta\Delta\left(1-\frac{x_b}{\Delta}\right)},\ \eta_d = \frac{1}{\eta\Delta\left(2-\frac{x_b}{\Delta}\right)},$$

$$\eta_e = \frac{1}{\eta\Delta\left(x_t - x_b - \frac{x_tx_b}{\Delta}\right)},\ \eta_f = \frac{1}{\eta\Delta\left(1+\frac{x_t}{\Delta}\right)^2},$$

and $\eta_g = \frac{1}{\eta\Delta\left(1-\frac{x_b}{\Delta}\right)^2}$.

Using Equation (1), the DQE at the output of the detector is

$$\mathrm{DQE} = \frac{\overline{\Phi}_3^2}{\overline{\Phi}_0(S_{N3}+S_{Ne})} \tag{14}$$

2.2. Folded Structure

The schematic diagram of a folded structure is shown in Figure 3, where the X-rays are attenuated along the y-axis and the X-ray generated charge carriers drift along the x-axis. The detail description of the folded structure was given in Ref. [13]. The quantum efficiency for the folded structure can be expressed as

$$\eta(E) = 1 - e^{-\alpha(E)l} \tag{15}$$

where l is photoconductor thickness.

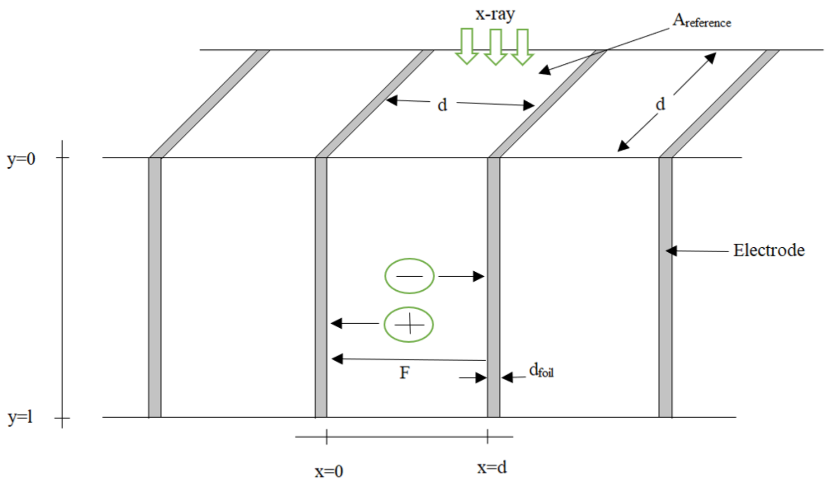

Figure 3. A folded detector structure where three pixels are shown.

The cascaded linear system model for calculating DQE of a folded structure has an additional stochastic gain stage, named as "effective filling" as shown in Figure 4.

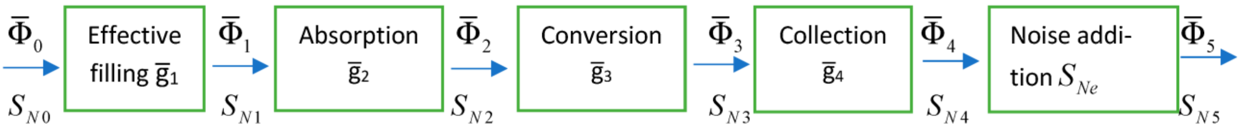

Figure 4. Cascaded linear system model for the folded structure of Figure 3.

The X-ray absorption in the electrode volume does not contribute to the EHP generation and this loss can be determined by the effective fill factor [13],

$$\overline{g}_1 = \frac{d}{d + d_{foil}} \tag{16}$$

where the width of the electrode is d_{foil}. The gain of this stage is g_1. Assuming a binomial selection process [13], the variance of gain $\sigma_{g1}^2 = \overline{g}_1(1 - \overline{g}_1)$.

Equations (6) and (7) are applicable for calculating the average charge collection $\overline{g}_4(x)$ and the variance of charge collection $\sigma_4^2(x)$ at the electrodes from EHP generation at coordinate x. However, the probability density function per unit area for an X-ray photon to interact at a distance y from the top electrode is,

$$p_{xy}(y) = \frac{\alpha}{\eta d} e^{-\alpha y} \; ; 0 \le y \le l \tag{17}$$

The total output signal after fourth stage,

$$\overline{\Phi}_4 = \eta \, \overline{\Phi}_0 \overline{g}_1 \overline{g}_3 \int_0^d \int_0^l \overline{g}_4(x) p_{xy}(y) dy dx = \eta \overline{\Phi}_0 \overline{g}_1 \overline{g}_3 \overline{\eta}_{cc} \tag{18}$$

where,

$$\overline{\eta}_{cc} = (x_t + x_b) - x_t{}^2\left(1 - e^{-\frac{1}{x_t}}\right) - x_b{}^2\left(1 - e^{-\frac{1}{x_b}}\right) \tag{19}$$

The NPS at the output of fourth stage is,

$$S_{N4} = \overline{\Phi}_0 \eta \overline{g}_1 \overline{g}_3 \int_0^d \int_0^l \left\{ \overline{g}_4^2(x)[1 + \overline{g}_3] + \sigma_{g_4}{}^2(x) \right\} p_{xy}(y) dy dx \tag{20}$$

$$\begin{aligned} S_{N4} = \overline{g}_3 \overline{g}_1 \overline{\Phi}_0 \eta (1 + \overline{g}_3) & \left[\begin{array}{c} x_t{}^2\left\{1 + 2x_t\left(e^{-\frac{1}{x_t}} - 1\right) - \frac{x_t}{2}\left(e^{-\frac{2}{x_t}} - 1\right)\right\} \\ +2x_t x_b\left\{1 + x_t\left(e^{-\frac{1}{x_t}} - 1\right) - x_b\left(1 - e^{-\frac{1}{x_b}}\right) + \frac{x_t x_b}{x_t - x_b}\left(e^{-\frac{1}{x_t}} - e^{-\frac{1}{x_b}}\right)\right\} \\ +x_b{}^2\left\{1 - 2x_b\left(1 - e^{-\frac{1}{x_b}}\right) + \frac{x_b}{2}\left(1 - e^{-\frac{2}{x_b}}\right)\right\} \end{array} \right] \\ +\overline{g}_3 \overline{g}_1 \eta \overline{\Phi}_0 & \left[\begin{array}{c} x_t{}^2\left\{1 + \frac{x_t}{2}\left(e^{-\frac{2}{x_t}} - 1\right) + 2e^{-\frac{1}{x_t}} + 2x_t\left(e^{-\frac{1}{x_t}} - 1\right)\right\} \\ +x_b{}^2\left\{1 + \frac{x_b}{2}\left(e^{-\frac{2}{x_b}} - 1\right) + 2e^{-\frac{1}{x_b}} + 2x_b\left(e^{-\frac{1}{x_b}} - 1\right)\right\} \end{array} \right] \end{aligned} \tag{21}$$

The DQE at the output (after fifth stage),

$$\text{DQE} = \frac{\overline{\Phi}_4^2}{\overline{\Phi}_0 (S_{N4} + S_{Ne})} \tag{22}$$

3. Result and Discussion

We have evaluated the DQE performance of poly-$MAPbI_3$ detectors having folded and conventional structures for both fluoroscopy and mammography applications. The thickness of the electrode in the folded structure is assumed to be d_{foil} = 2.8 µm [13]. The electric field has been taken to be F = 1 V/µm. The average photon energies for fluoroscopy and mammographic applications are assumed to be 60 keV and 20 keV, respectively. The range of exposure varies from 0.1 to 10 µR with the mean exposure being 1 µR in Fluoroscopy whereas it varies from 0.6 to 240 mR with the mean exposure being 12 mR in mammography [21].

The carrier transport properties (mobility and lifetime) of electrons and holes are very similar (within one order of magnitude) in perovskite materials [22]. For simplicity, both electron and hole mobility-lifetimes are assumed to be equal in poly-$MAPbI_3$ for theoretical calculations in this paper. We have varied the $\mu\tau$ values from 10^{-5} cm^2/V to 10^{-7} cm^2/V, which are reasonable for poly-$MAPbI_3$ [5]. The pixel size for fluoroscopic image sensors is large and the total electronic noise (N_e) typically varies from 1000 e to 2000 e per pixel whereas it varies from 500 e to 1000 e per pixel in mammographic detectors due to their smaller pixel size and the use of CMOS or active pixel technology [23]. The noise power, $S_{\text{Ne}} = N_e{}^2$.

The DQE of a folded structure for fluoroscopy applications as function of photoconductor thickness l and electrode distance d is shown in Figure 5. The exposure X = 1 µR and $\mu\tau = 10^{-6}$ cm^2/V. The pixel area is assumed as $d \times d$. The DQE increases monotonously with increasing the photoconductor thickness. The DQE should increase by increasing the distance between electrodes up to a certain value. Because the pixel area increases by increasing d and thus each pixel receives more signal, which overcomes the adverse effect of electronic noise per pixel. However, the DQE should decrease after a certain value of d when the charge collection efficiency decreases significantly and affects the signal to noise ratio. In Figure 5b, as d increases, the DQE first increases, reaches a maximum value at d = 0.015 cm, and then decreases afterward (d > 0.015 cm).

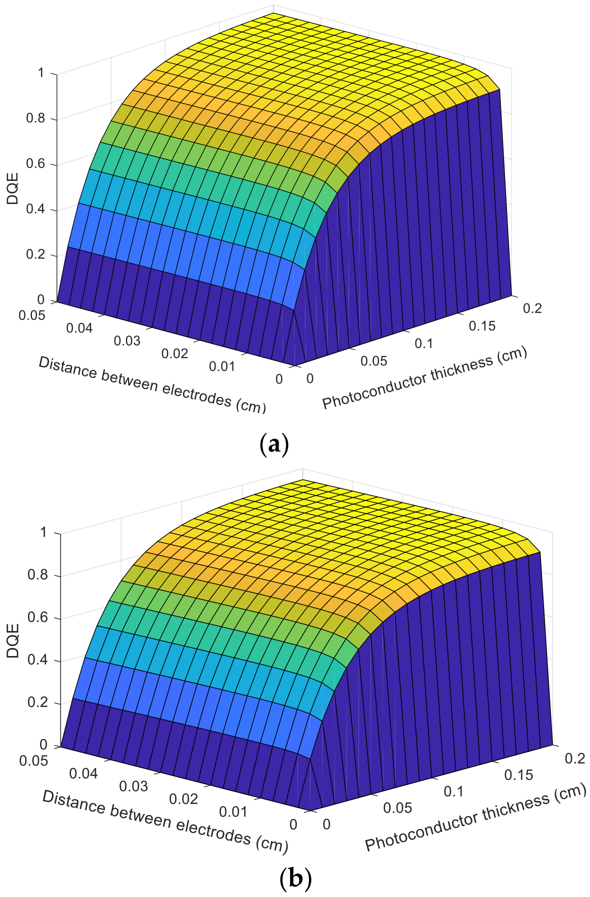

Figure 5. The DQE of a poly-MAPbI$_3$ folded X-ray detector for fluoroscopic applications. (**a**) $\mu\tau$ = 10^{-6} cm^2/V, X = 1 µR, N_e = 1000 e, and (**b**) $\mu\tau$ = 10^{-6} cm^2/V, X = 1 µR, N_e = 2000 e.

The optimum values of l and d for maximizing the DQE under various combinations of exposure, electronic noise and $\mu\tau$ are summarized in Table 1. The optimum DQE is more than 0.8 for all the possible combinations except for $\mu\tau$ = 10^{-7} cm^2/V. The optimum value of l varies within a very narrow range, i.e., from 0.06 to 0.1 cm, whereas the optimum value of d varies widely based on different situations.

Table 1. The optimum values of l and d for maximizing the DQE under various combinations of exposure, electronic noise and $\mu\tau$ of a folded poly-MAPbI$_3$ X-ray detector for fluoroscopic applications. The average photon energy E = 60 keV.

		X = 0.1 µR			X = 10 µR		
Electronic Noise	$\mu\tau$ **(cm^2/V)**	l **(cm)**	d **(cm)**	**DQE**	l **(cm)**	d **(cm)**	**DQE**
1000 e	10^{-5}	>0.07	0.025–0.5	>0.8	>0.07	0.025–0.5	>0.8
	10^{-6}	>0.07	0.025–0.1	>0.8	>0.07	0.025–0.5	>0.8
	10^{-7}	>0.1	0.0025–0.01	>0.8	>0.07	0.025–0.125	>0.8
2000 e	10^{-5}	>0.07	0.025–0.5	>0.8	>0.06	0.025–0.5	>0.8
	10^{-6}	>0.08	0.0025–0.045	>0.8	>0.07	0.025–0.5	>0.8
	10^{-7}	>0.08	0.0025–0.005	>0.7	>0.07	0.0025–0.05	>0.8

Figure 6 shows the DQE of a folded structure for mammographic applications. The exposure X = 3 mR, $\mu\tau$ = 10^{-6} cm^2/V. Table 2 shows the optimum values of l and d for maximizing the DQE under various combinations of exposures, electronic noise and μτ. The DQE increases with increasing *l* and *d* (up to *d* = 0.1 cm). The value of *l* should be greater than 0.01 cm whereas the optimum value *d* varies widely based on different operating conditions.

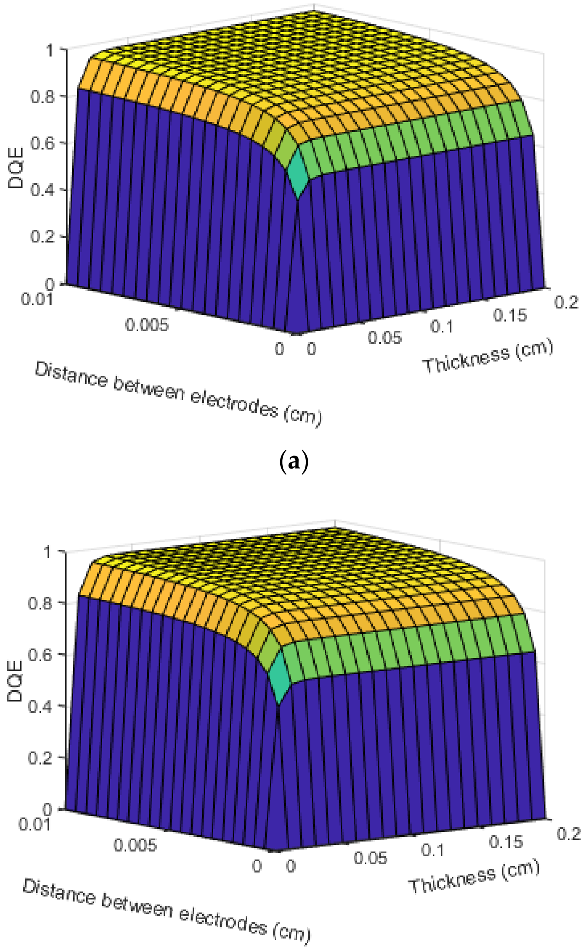

(**a**)

(**b**)

Figure 6. The DQE of a poly-$MAPbI_3$ folded X-ray detector for mammographic applications. (**a**) $\mu\tau = 10^{-6}$ cm^2/V, X = 3 mR, N_e = 500 e, and (**b**) $\mu\tau = 10^{-6}$ cm^2/V, X = 3 mR, N_e = 1000 e.

Table 2. The optimum values of *l* and *d* for maximizing the DQE under various combinations of exposure, electronic noise and $\mu\tau$ of a folded poly-$MAPbI_3$ X-ray detector for mammographic applications. The average photon energy *E* = 20 keV.

		X = 0.6 mR			X = 240 mR		
Electronic Noise	**$\mu\tau$ (cm^2/V)**	***l* (cm)**	***d* (cm)**	**DQE**	***l* (cm)**	***d* (cm)**	**DQE**
500 e	10^{-5}	>0.01	0.025–0.5	>0.8	>0.01	0.025–0.5	>0.8
	10^{-6}	>0.01	0.025–0.5	>0.8	>0.01	0.025–0.5	>0.8
	10^{-7}	>0.01	0.0025–0.05	>0.8	>0.01	0.025–0.05	>0.8
1000 e	10^{-5}	>0.01	0.025–0.5	>0.8	>0.01	0.025–0.5	>0.8
	10^{-6}	>0.01	0.025–0.325	>0.8	>0.01	0.025–0.5	>0.8
	10^{-7}	>0.01	0.0025–0.0325	>0.8	>0.01	0.025–0.5	>0.8

The effects of various parameters such as electronic noise, charge carrier transport properties, electric field, detector thickness on DQE performance of conventional structures are explained in previous publications [8,12]. For making a comparison, the DQE performance of conventional detectors for fluoroscopic and mammographic applications are shown in Figure 7. The exposure $X = 1$ µR and $F = 1$ V/µm. The DQE increases with increasing d, reaches a maximum value, and then decreases with further increasing d. There exists an optimum detector thickness (note the spacing between the two electrodes and the detector thickness are the same in conventional detector structure) for which the DQE is maximum. However, the optimum detector thickness and the maximum DQE depend on various parameters as evident from Figure 7. For example, unlike folded structure, the DQE can be less than 0.5 for higher electronic noise together with lower $\mu\tau$ values.

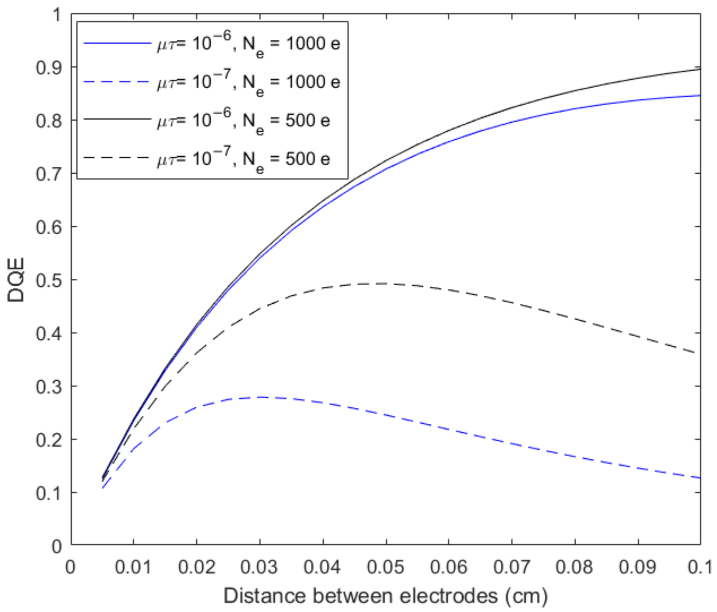

Figure 7. The DQE of a poly-$MAPbI_3$ conventional X-ray detector for fluoroscopic applications. The exposure $X = 1$ µR and $E = 60$ keV. The unit of $\mu\tau$ is cm^2/V.

In Table 3, we have gathered information about the optimum distance between electrodes d in different conditions in conventional detector structures for fluoroscopic applications. Unlike the folded structure, the optimum DQE for certain combinations of N_e and $\mu\tau$ can be even lower than 0.3, which is unacceptable for medical imaging.

Table 3. The optimum detector thickness for maximizing DQE under various combinations of exposure, electronic noise and $\mu\tau$ of a conventional poly-$MAPbI_3$ X-ray detector for fluoroscopic applications. The average photon energy $E = 60$ keV.

	X = 0.1 µR			X = 10 µR	
Electronic Noise	**$\mu\tau$ (cm^2/V)**	**d (cm)**	**DQE**	**d (cm)**	**DQE**
1000 e	10^{-5}	0.1	0.92	0.1	0.9307
	10^{-6}	0.09	0.7643	0.1	0.9109
	10^{-7}	0.02	0.1657	0.095	0.8048
2000 e	10^{-5}	0.1	0.889	0.1	0.9304
	10^{-6}	0.065	0.5728	0.1	0.9055
	10^{-7}	0.015	0.061	0.065	0.6335

Figure 8 shows the DQE performance of conventional detector for mammographic applications. The optimum detector thickness is in the range of 0.02 to 0.04 cm and the optimum DQE is larger than 0.9. In Table 4, we have gathered information about the optimum distance between electrodes d under various operating conditions in conventional structures for mammographic applications.

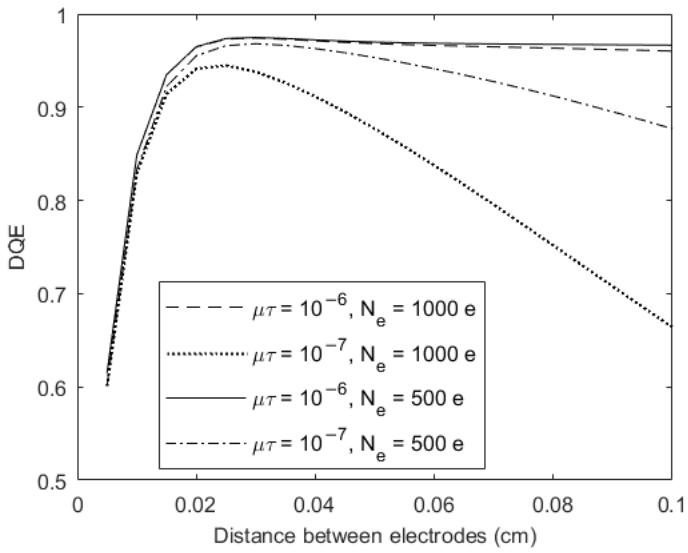

Figure 8. The DQE of a poly-$MAPbI_3$ conventional X-ray detector for mammographic applications. The exposure X = 3 mR and E = 20 keV. The unit of $\mu\tau$ is cm^2/V.

Table 4. The optimum detector thickness for maximizing DQE of a conventional poly-$MAPbI_3$ x-ray detector for mammographic applications under various combinations of exposure, electronic noise and $\mu\tau$. The average photon energy E = 60 keV.

		X = 0.6 mR		**X = 240 mR**	
Electronic Noise	**$\mu\tau$ (cm^2/V)**	**d (cm)**	**DQE**	**d (cm)**	**DQE**
500 e	10^{-5}	0.05	0.9984	0.05	0.9987
	10^{-6}	0.03	0.9739	0.03	0.9751
	10^{-7}	0.025	0.9379	0.06	0.9812
1000 e	10^{-5}	0.05	0.9975	0.06	0.9986
	10^{-6}	0.03	0.9705	0.03	0.9751
	10^{-7}	0.015	0.8738	0.04	0.9804

From the above discussion, we see that the DQE critically depends on the detector thickness. As a result, the optimum DQE can be even below 0.3 for certain values of material and device parameters in conventional structure. On the contrary, the folded structure provides more design flexibility for achieving high DQE (even higher than 0.7) by adjusting the distance between electrodes without compromising the quantum efficiency. Since the folded structure is more complex than the conventional structure, one should prefer the folded structure if the photoconductor possesses relatively low linear attenuation coefficient for higher energy X-rays together with poor charge carrier transport properties. Although the model has been applied to perovskite materials, this model and analysis can also be applied to other X-ray photoconductors (e.g., a-Se) as well. One can get similar results for other materials if the material possesses similar transport properties. Most of the X-ray photoconductors have quite similar transport properties as described in a recent book chapter [5].

The $\mu\tau$ values of electrons and holes are considered equal but varied quite widely (within two orders of magnitude) in the calculations. One can easily perform the same calculation considering the actual unequal $\mu\tau$ values. The charge collection efficiency will not change very significantly if $\mu\tau$ values of electrons and holes are within one order of magnitude [12] (this is the case in perovskite materials). Therefore, the main findings of this paper (summarised in previous paragraph) will not qualitatively differ.

4. Conclusions

The DQE performance of both folded and conventional detector structures has been analyzed by considering the quantum noise due to random charge carrier trapping in the photoconductor layer in the cascaded linear system model. An analytical expression for the variance of incomplete charge collection in folded structure has also been developed. The optimum values of photoconductor layer thickness l and spacing between electrodes d for maximizing the DQE under various combinations of exposure, electronic noise and $\mu\tau$ have been determined. The folded structure provides design flexibility for achieving DQE higher than 0.7 by adjusting the distance between electrodes while the maximum possible DQE in conventional structure can be even below 0.3 for certain values of material and detector parameters. The DQE model for folded structure in this paper can also be applied to coplanar detector structure if the electric field profile is considered uniform. This model and analysis of this paper can also be applied to other photoconductive detectors (e.g., *a*-Se detectors) as well.

Author Contributions: Conceptualization, M.Z.K.; Formal analysis, R.R. and M.Z.K.; Funding acquisition, M.Z.K.; Investigation, R.R. and M.Z.K.; Methodology, R.R. and M.Z.K.; Project administration, M.Z.K.; Resources, M.Z.K.; Software, R.R.; Supervision, M.Z.K.; Visualization, R.R.; Writing—original draft, R.R. and M.Z.K.; Writing—review & editing, M.Z.K. All authors have read and agreed to the published version of the manuscript.

Funding: This research was funded by Natural Science and Engineering Research Council of Canada, grant number RGPIN-2019-05472 and the APC was fully waived to the corresponding author (M. Z. Kabir).

Data Availability Statement: The data presented in this study are available in this article.

Conflicts of Interest: The authors declare no conflict of interest.

References

1. Spahn, M. X-ray detectors in medical imaging. *Nucl. Instr. Methods Phys. Res. Sect. A* **2013**, *731*, 57–63. [CrossRef]
2. Rowlands, J.A.; Zhao, W. Towards a digital radiology roadmap. *ECS Trans.* **2013**, *54*, 293–303. [CrossRef]
3. Cowen, A.R.; Davies, A.G.; Sivananthan, M.U. The design and imaging characteristics of dynamic, solid-state, flat-panel x-ray image detectors for digital fluoroscopy and fluorography. *Clin. Radiol.* **2008**, *63*, 1073–1085. [CrossRef] [PubMed]
4. Schlosser, D.M.; Huth, M.; Hartmann, R.; Abboud, A.; Send, S.; Conka-Nurdan, T.; Shokr, M.; Pietsch, U.; Strüder, L. Direct and indirect signal detection of 122 keV photons with a novel detector combining a pnCCD and a CsI (Tl) scintillator. *Nucl. Instr. Meth. Phys. Res. Sect. A* **2016**, *805*, 55–62. [CrossRef]
5. Kabir, M.Z. X-ray Photoconductivity and Typical Large Area X-ray Photoconductors. In *Photoconductivity and Photoconductive Materials*; Kasap, S.O., Ed.; Wiley & Sons: Chichester, UK, 2022; Chapter 15.
6. Kasap, S.; Frey, J.B.; Belev, G.; Tousignant, O.; Mani, H.; Greenspan, J.; Laperriere, L.; Bubon, O.; Reznik, A.; DeCrescenzo, G.; et al. Amorphous and Polycrystalline Photoconductors for Direct Conversion Flat Panel X-ray Image Sensors. *Sensors* **2011**, *11*, 5112–5157. [CrossRef] [PubMed]
7. Yakunin, S.; Sytnyk, M.; Kriegner, D.; Shrestha, S.; Richter, M.; Matt, G.; Azimi, H.; Brabec, C.; Stangl, J.; Kovalenko, M.; et al. Detection of X-ray photons by solution-processed lead halide perovskites. *Nat. Photonics* **2015**, *9*, 444. [CrossRef] [PubMed]
8. Kim, Y.C.; Kim, K.H.; Son, D.Y.; Jeong, D.N.; Seo, J.Y.; Choi, Y.S.; Han, I.T.; Lee, S.Y.; Park, N.G. Printable organometallic perovskite enables large-area, low-dose X-ray imaging. *Nature* **2017**, *550*, 87. [CrossRef] [PubMed]
9. Deumel, S.; van Breemen, A.; Gelinck, G.; Peeters, B.; Maas, J.; Verbeek, R.; Shanmugam, S.; Akkerman, H.; Meulenkamp, E.; Huerdler, J.E.; et al. High-sensitivity high-resolution X-ray imaging with soft-sintered metal halide perovskites. *Nat. Electron.* **2021**, *4*, 681–688. [CrossRef]

10. Li, Y.; Adeagbo, E.; Koughia, C.; Simonson, B.; Pettipas, R.D.; Mishchenko, A.; Arnab, S.M.; Laperrière, L.; Belev, G.; Stevens, A.L.; et al. Direct conversion X-ray detectors with 70 pA cm^{-2} dark currents coated from an alcohol-based perovskite ink. *J. Mater. Chem. C* **2022**, *10*, 1228–1235. [CrossRef]
11. Kabir, M.Z.; Kasap, S. Modulation transfer function of photoconductive X-ray image detectors: Effects of charge carrier trapping. *J. Phys. D Appl. Phys.* **2003**, *36*, 2352–2358. [CrossRef]
12. Kabir, M.Z.; Kasap, S. DQE of photoconductive x-ray image detectors: Application to a-Se. *J. Phys. D Appl. Phys.* **2002**, *35*, 2735–2743. [CrossRef]
13. Mescher, H.; Hamann, E.; Lemmer, U. Simulation and design of folded perovskite X-ray detectors. *Sci. Rep.* **2019**, *9*, 5231. [CrossRef] [PubMed]
14. Hunter, D.M.; Rowlands, J.A. Differences between transient photoconductivity in a-Se sandwich(bulk) and co-planar(interface) structures. *J. Mater. Sci. Mater. Electron.* **2020**, *31*, 9114–9125. [CrossRef]
15. Mainprize, J.G.; Hunt, D.C.; Yaffe, M.J. Direct conversion detectors: The effect of incomplete charge collection on detective quantum efficiency. *Med. Phys.* **2002**, *29*, 976–990. [CrossRef] [PubMed]
16. Rabbani, M.; Shaw, R.; Van Metter, R. Detective quantum efficiency of imaging systems with amplifying and scattering mechanisms. *J. Opt. Soc. Am. A* **1987**, *4*, 895–901. [CrossRef] [PubMed]
17. Cunningham, I. Applied linear-systems theory. In *Handbook of Medical Imaging*; Beutel, J., Kundel, H.L., Van Metter, R.L., Eds.; SPIE Press: Washington, DC, USA, 2000; Volume 1, Chapter 2.
18. Zhao, W.; Ji, W.G.; Debrie, A.; Rowlands, J.A. Imaging performance of amorphous selenium based flat-panel detectors for digital mammography: Characterization of a small area prototype detector. *Med. Phys.* **2003**, *30*, 254–263. [CrossRef] [PubMed]
19. Kabir, M.Z.; Emelianova, E.V.; Arkhipov, V.I.; Yunus, M.; Adriaenssens, G.; Kasap, S.O. The effects of large signals on charge collection in radiation detectors: Application to amorphous selenium detectors. *J. Appl. Phys.* **2006**, *99*, 124501. [CrossRef]
20. Kabir, M.Z. Effects of charge carrier trapping on polycrystalline PbO X-ray imaging detectors. *J. Appl. Phys.* **2008**, *104*, 074506. [CrossRef]
21. Rowlands, J.; Yorkston, J. Flat panel detectors for digital radiography. In *Handbook of Medical Imaging: Volume 1*; Beutel, J., Kundel, H.L., Van Metter, R.L., Eds.; SPIE Press: Washington, DC, USA, 2000; Chapter 4.
22. Ball, J.M.; Petrozza, A. Defects in perovskite-halides and their effects in solar cells. *Nat. Energy* **2016**, *1*, 16149. [CrossRef]
23. Kabir, M.Z. Basic principles of solid state X-ray radiation detector operation. In *Handbook of II–VI Semiconductor-Based Sensors and Radiation Detectors: Volume 3 Sensors—Biosensors and Radiation Detectors*; Korotcenkov, G., Ed.; Springer Nature: Cham, Switzerland, 2023; Chapter 1.